

Article

Not peer-reviewed version

Disturbance Rejection Control of Grid-Forming Inverter for Line Impedance Parameter Perturbation in Weak Power Grid

[Mayue Huang](#) and [Hui Li](#)*

Posted Date: 24 April 2024

doi: 10.20944/preprints202404.1516.v1

Keywords: grid-forming inverter; power decoupling; reduced-order extended state observer; dynamic phasor method; virtual impedance; line impedance parameter perturbation



Preprints.org is a free multidiscipline platform providing preprint service that is dedicated to making early versions of research outputs permanently available and citable. Preprints posted at Preprints.org appear in Web of Science, Crossref, Google Scholar, Scilit, Europe PMC.

Copyright: This is an open access article distributed under the Creative Commons Attribution License which permits unrestricted use, distribution, and reproduction in any medium, provided the original work is properly cited.

Article

Disturbance Rejection Control of Grid-Forming Inverter for Line Impedance Parameter Perturbation in Weak Power Grid

Mayue Huang and Hui Li *

College of Automation Engineering, Shanghai University of Electric Power, Shanghai 200090, China; huangml98@outlook.com

* Correspondence: lihui@shiep.edu.cn

Abstract: When a grid-forming (GFM) inverter is connected to a low or medium voltage weak power grid, the line impedance with resistive-inductive characteristics will cause power coupling. Typical GFM decoupling control strategies are designed under nominal line impedance parameters. However, there are deviations between the nominal line impedance and actual parameters, resulting in poor decoupling effects. Aiming at this problem, this paper proposes a power decoupling strategy based on a reduced-order extended state observer (ESO). Firstly, the power dynamic model of GFM is established based on the dynamic phasor method. Then, the model deviation and power coupling due to line impedance parameter perturbation are estimated as internal disturbances of the system, and the disturbances are compensated on the basis of typical power control strategy and virtual impedance decoupling. Good decoupling performance is obtained under different impedance parameters, improving the control strategy's robustness. Finally, the effectiveness of the proposed method is verified by the results of RT Box hardware-in-the-loop experiments.

Keywords: grid-forming inverter; power decoupling; reduced-order extended state observer; dynamic phasor method; virtual impedance; line impedance parameter perturbation

1. Introduction

Conventional fossil energy sources are connected to the grid through Synchronous Generators (SGs), and the presence of a large number of SGs slows down the dynamics of the entire system [1]. With a large number of new energy sources connected to the power system, the proportion of inverter-based power source (IBPS) power generation in the grid has been increasing, replacing most of the SGs and becoming an important trend in the development of the power system [2]. Conventional grid-following (GFL) inverters are synchronized with the grid through the phase-locked loop (PLL), and their proper operation relies on the presence of a voltage source in the system to build a voltage reference. However, more IBPSs also lead to faster system dynamics, and the stable operation of the GFL will be affected, resulting in a lack of voltage support and inertial responsiveness of the grid [3,4].

As a new solution, grid-forming inverter has been proposed and widely and deeply researched [5–8]. By simulating the characteristics of a synchronous generator, GFM applies the rotor motion equations of the synchronous generator and the primary frequency modulation to the control of the inverter [9] so that the external characteristics of the inverter present the inertia and damping characteristics similar to those of the synchronous generator [10]. The system voltage and frequency can be established independently [11,12], thus effectively improving the stability of the power system [13]. In the GFMs above, it is assumed that the impedance of the line is purely inductive, and this assumption is consistent with the case of high-voltage grids. After connecting to the low and medium

voltage weak grid, the line impedance ratio R/X is relatively large, so there is a significant coupling between active power and reactive power [14].

Power modeling is the basis of theoretical analysis. There are mainly steady-state models and dynamic models. In [15–17], the steady-state models of active and reactive power were established to analyze the GFM's stability and to design power control parameters, respectively. The transfer function of the steady-state model is constant and cannot reflect the dynamic characteristics of the line impedance. The dynamic models of active and reactive power are developed in [18] and [19]. Due to the low bandwidth of the power control loop, the analysis with the steady state model also yields results consistent with those analyzed with the dynamic model. However, the power coupling involves transient processes, and it is more appropriate to use the dynamic model. This paper uses the dynamic phasor method [20] to develop a dynamic model that can more accurately describe system behavior during unsteady state or transient processes.

In order to solve the power coupling problem, many scholars have conducted a series of research studies. In [21–23], the virtual power method is used for power decoupling. Based on the impedance angle of the line impedance, the active and reactive power coordinates are transformed into virtual active and reactive power, which are controlled by frequency and voltage magnitude, respectively. However, implementing this method is subject to the accurate acquisition of the resistance-inductance ratio in the line. In [24,25], voltage and frequency cross-channel feedforward compensation methods are proposed for droop control and virtual synchronous generator (VSG), respectively. In [26], a reactive power feedforward compensation method is proposed to reduce power coupling. Similar problems exist with the virtual power method, as feedforward decoupling requires knowledge of the exact line impedance parameters and the power angle of the GFM. The most common power decoupling method is through the reconstruction of the inverter output impedance by the virtual impedance method [27,28]. In [29], a strategy to introduce virtual inductance in the control system was proposed based on increasing the neutral inductive component of the line impedance, which effectively reduces the power coupling between active and Q reactive power. However, it is pointed out in [30] that the power decoupling capability is somewhat constrained due to the inherent d -axis voltage drop caused by the virtual inductor. A virtual negative resistance approach was introduced in [31] that reduces the resistive characteristics of the line impedance. As a result, the line impedance is inductive, and the coupling between P and Q is reduced.

An easily overlooked issue in existing studies is that the variation of line impedance is not considered. If a parameter perturbation in the line impedance causes it to deviate from the nominal value, the power decoupling performance worsens. In [32], a total sliding-mode controller (TSMC) is used for power decoupling, and excellent decoupling performance can be obtained when the line impedance varies in a small range. However, the jitter phenomenon restricts the robustness of the power decoupling, and the stronger the robustness, the worse the jitter phenomenon. In [33], a feedforward neural network (FNN) framework is used to simulate the TSMC law for robust and accurate decoupling control. The simulation and experimental results verify the robustness of power decoupling, but the design of the control system is complex and cannot be implemented on a microcontroller. In [34], a power decoupling strategy based on an extended state observer is proposed. On the basis of the feedforward decoupling method, the power coupling is estimated as an internal disturbance of the system using an extended state observer (ESO), and the output of the feedforward decoupling method is compensated to improve the robustness of the feedforward decoupling method. Feedforward decoupling can make the strongly coupled channel paired and the weakly coupled channel decoupled. However, when the resistive component of the line impedance is larger than the inductive component, the P - δ and Q - E control channels are weakly coupled, which does not satisfy the principle of optimal pairing of the control channels.

Therefore, this paper proposes a power decoupling strategy based on a reduced-order extended state observer (RESO). The factors affecting the power control performance, such as model deviation and power coupling caused by line impedance parameter perturbation, are considered internal disturbances. These disturbances are observed in real time by a RESO, and the disturbance compensation is performed based on the virtual impedance decoupling method. Good decoupling

performance is obtained even under different impedance parameters, and the robustness of virtual impedance decoupling is improved. The main contributions of this paper are as follows:

A small-signal model of the power dynamics of GFM is established based on the dynamic phasor method, and according to the small-signal model, the disturbances existing in the power control of GFM after considering the line impedance parameter perturbation are analyzed.

A power decoupling strategy based on RESO is proposed. The reduced-order ESO reduces the amount of control system arithmetic and the system's phase delay. Good decoupling performance can be obtained even under different impedance parameters, and the robustness of the virtual impedance decoupling method is improved.

The transfer functions of the disturbance estimation capability and disturbance estimation error of two ESOs are derived, and the disturbance estimation capability of two ESOs and the disturbance estimation capability of RESO under different observation bandwidths are analyzed.

The organizational structure of this paper is as follows: Section 2 introduces typical control strategies for grid-forming inverters and analyses the disturbance after considering the line impedance parameter perturbation; Section 3 proposes the design of a power decoupling control strategy based on a reduced-order ESO and analyses the performance of ESO disturbance estimation; Section 4 illustrates the hardware-in-the-loop experimental results; Section 5 provides the conclusion.

2. Typical Control and Disturbance Analyses of Grid-Forming Inverters

2.1. Typical Control Strategies for Grid-Forming Inverters

The central circuit topology and control block diagram of the grid-forming inverter are shown in Figure 1. The DC source is connected to the AC grid using a three-phase voltage source inverter, and the system as a whole consists of a DC-side equivalent power supply, an inverter bridge, an LCL-type filter, an equivalent line impedance, and a grid configuration. Among them, L_1 is the inverter-side inductance; C is the filter capacitance; L_2 is the grid-side inductance; R_g and L_g are the equivalent line resistance and inductance between the GFM and the grid; u_{dc} is the DC bus voltage, u_x is the inverter bridge arm voltage, i_x is the inverter-side inductance current, u_{2x} is the inverter output voltage, i_{2x} is the inverter output current, and u_{gx} is the grid voltage ($x = a, b, c$); E is the virtual internal potential of the VSG; δ is the virtual rotor angle, generated by the virtual angular frequency ω .

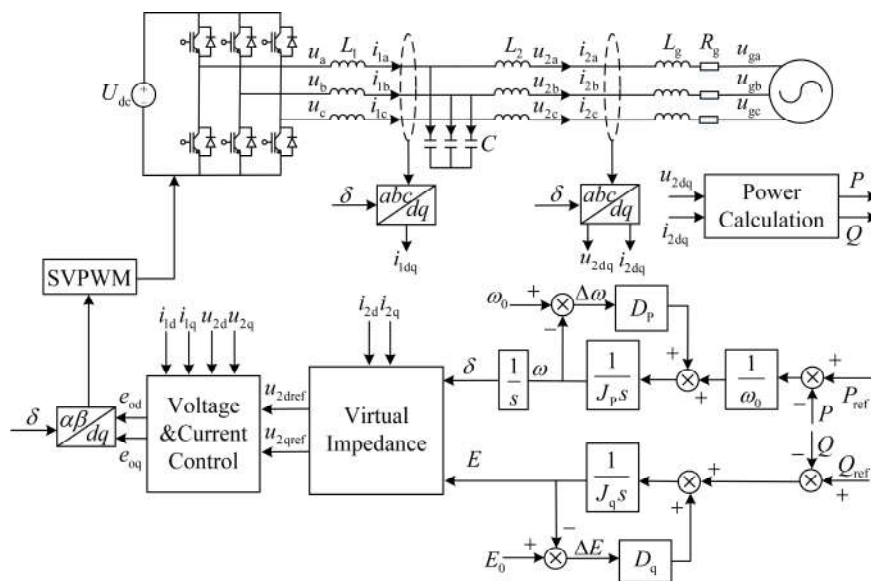


Figure 1. Central circuit topology and typical control block diagram of grid-forming inverter.

In the power control of the grid-forming inverter, the power control link of the virtual synchronous machine plays a crucial role. It consists of two main parts, active and reactive power control, as shown in Figure 1. The active power control link is realized by simulating the real rotor's equations of motion and the prime mover's speed governing equations, using P - ω for control. The specific expression is shown in Equation (1).

$$\frac{P_{\text{ref}}}{\omega_0} - \frac{P}{\omega_0} - D_p (\omega - \omega_0) = J_p \frac{d\omega}{dt} \quad (1)$$

where J_p and D_p are the active virtual inertia and droop coefficient of the VSG, respectively; P_{ref} and P are the active power setpoint and the actual active power output from the inverter, respectively; ω_0 and ω are the rated and actual output angular frequency of the VSG, respectively.

The reactive power control link adopts Q - E control by simulating the voltage regulation characteristics of the synchronous generator, thus generating the magnitude of the virtual internal potential, with the specific expression shown in Equation (2).

$$Q_{\text{ref}} - Q + D_q (E_0 - E) = J_q \frac{dE}{dt} \quad (2)$$

where J_q and D_q are the virtual inertia coefficient and droop coefficient of VSG reactive power, respectively; Q_{ref} and Q are the set value of reactive power and the actual output reactive power, respectively; and E_0 is the peak value of the rated output voltage of VSG.

Considering that the virtual steady-state synchronous complex impedance control can significantly reduce the output impedance of the GFM in the high-frequency range, which further improves the stability of the system, the power decoupling control is carried out based on the virtual steady-state synchronous complex impedance. The mathematical expression of the virtual impedance control link in the dq coordinate system is given by:

$$\begin{cases} u_{2\text{dref}} = E - R_v i_{2\text{d}} + X_v i_{2\text{q}} \\ u_{2\text{qref}} = 0 - R_v i_{2\text{q}} - X_v i_{2\text{d}} \end{cases} \quad (3)$$

where R_v and X_v are the virtual resistance and virtual reactance of the GFM, respectively, $X_v = \omega_0 L_v$, and L_v is the virtual inductance.

The voltage-current control is controlled by inner-loop inductor current P control and outer-loop output voltage PI control. After the compensation of the virtual impedance link, the voltage reference value is fed into the voltage-current double closed loop to achieve the fast-tracking of the GFM output voltage. Finally, the modulating waves e_{od} and e_{oq} are fed into the SVPWM link for modulation to drive the inverter bridge.

2.2. Disturbance Analysis after Considering Line Impedance Parameter Perturbation

In order to ensure a suitable voltage-following capability for output voltage control, the bandwidth of the voltage-current dual-loop closure is set to be much larger than that of the external power control loop. As a result, the VSG-controlled GFM can be simplified as a controllable voltage source [27]. After introducing the virtual impedance control, the equivalent circuit diagram of its access to the AC grid is shown in Figure 2. Where E is the virtual internal potential amplitude of the VSG; δ is the phase difference between the virtual internal potential of the VSG and the grid voltage, which is the power angle; U_o and δ_o are the voltage amplitude at the output of the GFM and the phase difference between the GFM output and the grid voltage, respectively, after virtual impedance compensation is performed; \tilde{S} , P and Q are the actual complex power, active power and reactive power output from the virtual synchronous machine, respectively.

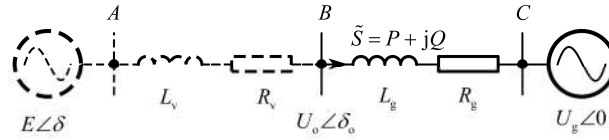


Figure 2. Grid-connected equivalent circuit diagram of GFM.

Conventional phase quantities are built on the assumption that the power electronic system is a quasi-steady state, which presupposes that the rate of change of the amplitude and phase of the system voltages, currents, and other physical quantities is much less than the system's base frequency angular velocity ω_0 . In a quasi-steady state, the amplitude within the frequency bandwidth $(-\omega_0, \omega_0)$ is considered to be constant. Therefore, the electrical quantities can be approximated as a sinusoidal waveform, which can be expressed in terms of the phase quantity method. However, in the dynamic phase volume concept, the phase volume change rate is close to the angular velocity of the fundamental frequency, although it is still less than that. At the same time, its frequency bandwidth is also close to, but less than, the fundamental frequency, and within this bandwidth, the amplitude is no longer constant but varies over a range. Thus, the dynamic phase can more accurately describe the system's behavior during unsteady or transient processes.

For inductive elements, the dynamic phase model [20] is:

$$\dot{U}_L = L \frac{d\dot{I}_L}{dt} + j\omega_0 L \dot{I}_L \quad (4)$$

where \dot{U}_L is denoted as the dynamic phase form of the variable u_L , which is the inductive voltage; \dot{I}_L is denoted as the dynamic phase form of the variable i_L , which is the inductive current.

When building the quasi-static model, it will be ignored that the differential terms of the dynamic phasors on the right side of the equal sign with respect to time are often neglected.

According to Figure 2 combined with Equation (4), the relationship between the GFM output voltage and output current I can be obtained as:

$$\begin{cases} \dot{E} - \dot{U}_o = (R_v + jX_v)\dot{I} \\ \dot{U}_o - \dot{U}_g = (R_g + jX_g)\dot{I} + L_g \frac{d\dot{I}}{dt} \end{cases} \quad (5)$$

Since the virtual impedance link is designed for steady-state synchronous impedance control, the differential term is not considered in the virtual impedance modeling.

Laplace transformation of Equation (5) and collation gives the current flowing into the grid as:

$$\dot{I} = \frac{E\angle\delta - U_o\angle\delta_o}{R_v + jX_v} = \frac{U_o\angle\delta_o - U_g\angle 0}{R_g + jX_g + sL_g} = \frac{E\angle\delta - U_g\angle 0}{R + jX + sL_g} \quad (6)$$

where $R=R_v+R_g$ and $X=X_v+X_g$. Then, the inverter output complex power can be found as:

$$\begin{aligned} \tilde{S} &= 3\dot{U}_o \cdot \dot{I}^* \\ &= P + jQ \\ &= 3[E\angle\delta - \dot{I}(R_v + j\omega L_v)] \cdot \dot{I}^* \\ &= 3[E\angle\delta \dot{I}^* - \dot{I} \dot{I}^*(R_v + j\omega L_v)] \end{aligned} \quad (7)$$

The actual output active power P and reactive power Q of the GFM considering the dynamic process can be obtained as:

$$P = \frac{3[R_v(EU_g \cos \delta - U_g^2) + (R_g + sL_g)(E^2 - EU_g \cos \delta) + XEU_g \sin \delta]}{(R + sL_g)^2 + X^2}$$

$$Q = \frac{3[X_v(EU_g \cos \delta - U_g^2) + X_g(E^2 - EU_g \cos \delta) - (R + sL_g)EU_g \sin \delta]}{(R + sL_g)^2 + X^2}$$
(8)

The output power expression of the GFM at (δ_0, E_0) , linearized and small-signal modeled, can be obtained by taking the partial derivatives for P and Q , respectively:

$$\begin{bmatrix} \Delta P \\ \Delta Q \end{bmatrix} = \left. \begin{bmatrix} \frac{\partial P}{\partial \delta} & \frac{\partial P}{\partial E} \\ \frac{\partial Q}{\partial \delta} & \frac{\partial Q}{\partial E} \end{bmatrix} \right|_{(\delta_0, E_0)} \begin{bmatrix} \Delta \delta \\ \Delta E \end{bmatrix} = G_v \begin{bmatrix} \Delta \delta \\ \Delta E \end{bmatrix}$$
(9)

Where

$$G_v(s) = \begin{bmatrix} G_{(v)P-\delta}(s) & G_{(v)P-E}(s) \\ G_{(v)Q-\delta}(s) & G_{(v)Q-E}(s) \end{bmatrix}$$

$$= \begin{bmatrix} \frac{k_{11}s + k_{12}}{g_1s^2 + g_2s + g_3} & \frac{k_{21}s + k_{22}}{g_1s^2 + g_2s + g_3} \\ \frac{k_{31}s + k_{32}}{g_1s^2 + g_2s + g_3} & \frac{k_{41}s + k_{42}}{g_1s^2 + g_2s + g_3} \end{bmatrix}$$
(10)

where the individual numerator denominator coefficients of the transfer function are:

$$\begin{cases} g_1 = L_g^2 \\ g_2 = 2L_g R \\ g_3 = R^2 + X^2 \\ k_{11} = E_0 U_g \sin \delta_0 L_g \\ k_{12} = E_0 U_g [\cos \delta_0 X + \sin \delta_0 (R_g - R_v)] \\ k_{21} = (2E_0 - U_g \cos \delta_0) L_g \\ k_{22} = U_g \cos \delta_0 (R_v - R_g) + 2E_0 R_g + U_g \sin \delta_0 X \\ k_{31} = -E_0 U_g \cos \delta_0 L_g \\ k_{32} = E_0 U_g [\sin \delta_0 (X_g - X_v) - \cos \delta_0 R] \\ k_{41} = -U_g \sin \delta_0 L_g \\ k_{42} = U_g \cos \delta_0 (X_v - X_g) + 2E_0 X_g - U_g \sin \delta_0 R \end{cases}$$
(11)

From Equation (11), the power dynamic small signal model of GFM is shown in Figure 3.

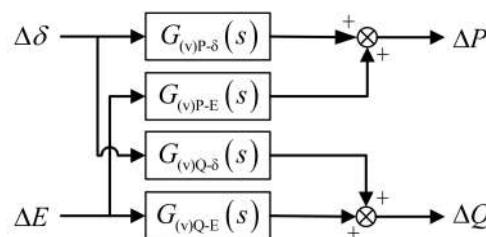


Figure 3. GFM Power small signal model (considering virtual impedance).

Rewriting the small-signal model in the time-domain progression can be obtained:

$$\begin{cases} \Delta\ddot{P} + \frac{\mathcal{G}_2}{\mathcal{G}_1} \Delta\dot{P} + \frac{\mathcal{G}_3}{\mathcal{G}_1} \Delta P = \frac{k_{12}}{\mathcal{G}_1} \Delta\delta + \frac{k_{11}}{\mathcal{G}_1} \Delta\dot{\delta} + \frac{k_{21}}{\mathcal{G}_1} \Delta\dot{E} + \frac{k_{22}}{\mathcal{G}_1} \Delta E \\ \Delta\ddot{Q} + \frac{\mathcal{G}_2}{\mathcal{G}_1} \Delta\dot{Q} + \frac{\mathcal{G}_3}{\mathcal{G}_1} \Delta Q = \frac{k_{42}}{\mathcal{G}_1} \Delta E + \frac{k_{41}}{\mathcal{G}_1} \Delta\dot{E} + \frac{k_{31}}{\mathcal{G}_1} \Delta\dot{\delta} + \frac{k_{32}}{\mathcal{G}_1} \Delta\delta \end{cases} \quad (12)$$

In actual working conditions, there is a parameter perturbation in the line impedance. Not only is there an accuracy error between the actual and nominal parameters of the components, but also, if the grid is affected by factors such as environment, electromagnetic interference, mechanical stress changes, etc., the line impedance parameters also deviate from the nominal value, and the effect of power decoupling will become worse. Therefore, the system can be separated according to Equation (13) as:

$$\begin{cases} \Delta\ddot{P} + \frac{\mathcal{G}_2^n}{\mathcal{G}_1^n} \Delta\dot{P} + \frac{\mathcal{G}_3^n}{\mathcal{G}_1^n} \Delta P = \left(\frac{\mathcal{G}_2^n}{\mathcal{G}_1^n} - \frac{\mathcal{G}_2}{\mathcal{G}_1} \right) \Delta\dot{P} + \left(\frac{\mathcal{G}_3^n}{\mathcal{G}_1^n} - \frac{\mathcal{G}_3}{\mathcal{G}_1} \right) \Delta P + \frac{k_{12}^n}{\mathcal{G}_1^n} \Delta\delta + \left(\frac{k_{12}^n}{\mathcal{G}_1^n} - \frac{k_{12}}{\mathcal{G}_1} \right) \Delta\delta \\ \quad + \frac{k_{11}}{\mathcal{G}_1} \Delta\dot{\delta} + \frac{k_{21}}{\mathcal{G}_1} \Delta\dot{E} + \frac{k_{22}}{\mathcal{G}_1} \Delta E \\ \Delta\ddot{Q} + \frac{\mathcal{G}_2^n}{\mathcal{G}_1^n} \Delta\dot{Q} + \frac{\mathcal{G}_3^n}{\mathcal{G}_1^n} \Delta Q = \left(\frac{\mathcal{G}_2^n}{\mathcal{G}_1^n} - \frac{\mathcal{G}_2}{\mathcal{G}_1} \right) \Delta\dot{Q} + \left(\frac{\mathcal{G}_3^n}{\mathcal{G}_1^n} - \frac{\mathcal{G}_3}{\mathcal{G}_1} \right) \Delta Q + \frac{k_{42}^n}{\mathcal{G}_1^n} \Delta E + \left(\frac{k_{42}^n}{\mathcal{G}_1^n} - \frac{k_{42}}{\mathcal{G}_1} \right) \Delta E \\ \quad + \frac{k_{31}}{\mathcal{G}_1} \Delta\dot{\delta} + \frac{k_{32}}{\mathcal{G}_1} \Delta\delta + \frac{k_{41}}{\mathcal{G}_1} \Delta\dot{E} \end{cases} \quad (13)$$

Where the coefficients with the label n indicate the use of nominal line impedance parameters, and the coefficients without the label n indicate the use of actual line impedance parameters. As the control structure between active and reactive power is similar, the active power ring control ring is analyzed as an example. Let:

$$\begin{cases} f_p = \left(\frac{\mathcal{G}_2^n}{\mathcal{G}_1^n} - \frac{\mathcal{G}_2}{\mathcal{G}_1} \right) \Delta\dot{P} + \left(\frac{\mathcal{G}_3^n}{\mathcal{G}_1^n} - \frac{\mathcal{G}_3}{\mathcal{G}_1} \right) \Delta P + \left(\frac{k_{12}^n}{\mathcal{G}_1^n} - \frac{k_{12}}{\mathcal{G}_1} \right) \Delta\delta + \frac{k_{11}}{\mathcal{G}_1} \Delta\dot{\delta} + \frac{k_{21}}{\mathcal{G}_1} \Delta\dot{E} + \frac{k_{22}}{\mathcal{G}_1} \Delta E \\ f = -\frac{\mathcal{G}_2^n}{\mathcal{G}_1^n} \Delta\dot{P} - \frac{\mathcal{G}_3^n}{\mathcal{G}_1^n} \Delta P + f_p \end{cases} \quad (14)$$

where f is the total disturbance and f_p is the disturbance without model information. The total disturbance f has several components, including: $\frac{k_{22}}{\mathcal{G}_1} \Delta E$ and $\frac{k_{21}}{\mathcal{G}_1} \Delta\dot{E}$ are the disturbances coupled

between active and reactive power after being compensated by virtual impedance; $\left(\frac{\mathcal{G}_2^n}{\mathcal{G}_1^n} - \frac{\mathcal{G}_2}{\mathcal{G}_1} \right) \Delta\dot{P}$,

$\left(\frac{\mathcal{G}_3^n}{\mathcal{G}_1^n} - \frac{\mathcal{G}_3}{\mathcal{G}_1} \right) \Delta P$ and $\left(\frac{k_{12}^n}{\mathcal{G}_1^n} - \frac{k_{12}}{\mathcal{G}_1} \right) \Delta\delta$ are the disturbances due to model deviation; $\frac{\mathcal{G}_2^n}{\mathcal{G}_1^n} \Delta\dot{P}$ and $\frac{\mathcal{G}_3^n}{\mathcal{G}_1^n} \Delta P$

are the model information of the system, which is a part of the model different from the integral series-type standard type, and are estimated together in the estimation of the total disturbances, but when power decoupling is performed, in order not to change the model of the original system, only the disturbances are compensated when compensates the disturbance f_p that does not contain the model information.

3. Decoupling Control Strategy of Grid-Forming Inverter Based on Reduced-Order ESO

3.1. Design of Reduced-Order ESO

Design the controller as an example of an active power loop control loop such that:

$$y = \Delta P, u = \Delta \delta, b_{p0} = \frac{k_{12}^n}{g_1^n}, a_1 = \frac{g_3^n}{g_1^n}, a_2 = \frac{g_2^n}{g_1^n} \quad (15)$$

The state variables are selected as follows:

$$\begin{cases} x_1 = y = \Delta P \\ x_2 = \dot{y} = \Delta \dot{P} \\ x_3 = f = -a_1 x_1 - a_2 x_2 + f_p \\ h = \dot{f} \end{cases} \quad (16)$$

The expansion equation of state for GFM active power can be obtained as:

$$\begin{cases} \begin{bmatrix} \dot{x}_1 \\ \dot{x}_2 \\ \dot{x}_3 \end{bmatrix} = \begin{bmatrix} 0 & 1 & 0 \\ 0 & 0 & 1 \\ 0 & 0 & 0 \end{bmatrix} \begin{bmatrix} x_1 \\ x_2 \\ x_3 \end{bmatrix} + \begin{bmatrix} 0 & 0 \\ b_{p0} & 0 \\ 0 & 1 \end{bmatrix} \begin{bmatrix} u \\ h \end{bmatrix} \\ y = x_1 \end{cases} \quad (17)$$

It can be seen through Equation (14) that the system is a second-order system and requires the design of a third order ESO to estimate the total disturbance f . The state equation is:

$$\begin{cases} \dot{z}_1 = z_2 + \beta_1 (x_1 - z_1) \\ \dot{z}_2 = z_3 + b_{p0} u + \beta_2 (x_1 - z_1) \\ \dot{z}_3 = \beta_3 (x_1 - z_1) \end{cases} \quad (18)$$

where $z_1, z_2,$ and z_3 are the real-time observations of the state variables $x_1, x_2,$ and x_3 , respectively, and $\beta_1, \beta_2,$ and β_3 are the observer gain matrices.

The performance of the ESO-based controller mainly depends on the accuracy of the state and disturbance estimation [35]. The higher the order of the ESO, the more obvious the hysteresis effect of the observed disturbances is [36], which affects the effectiveness of the compensation of the disturbance f_p . Since the output voltage and current of the grid-forming inverter can be obtained through sensors and the output power of the inverter is calculated. Therefore, the structure of ESO, by observing the output power, can be deleted, and a RESO can be used to reduce the complexity of the algorithm. Equation (17) can be transformed into:

$$\begin{cases} \begin{bmatrix} \dot{x}_2 \\ \dot{x}_3 \end{bmatrix} = \begin{bmatrix} 0 & 1 \\ 0 & 0 \end{bmatrix} \begin{bmatrix} x_2 \\ x_3 \end{bmatrix} + \begin{bmatrix} b_{p0} & 0 \\ 0 & 1 \end{bmatrix} \begin{bmatrix} u \\ h \end{bmatrix} \\ y = x_2 \end{cases} \quad (19)$$

RESO can be designed to:

$$\begin{cases} \dot{z}_2 = z_3 + b_{p0} u + l_2 (x_2 - z_2) \\ \dot{z}_3 = l_3 (x_2 - z_2) \end{cases} \quad (20)$$

where l_2 and l_3 are the reduced-order observer gain matrices are the observer gains. RESO requires the differentiation of ΔP , which introduces high-frequency noise into the control loop and adversely affects the control effectiveness. Therefore, the ESO must be reconstructed to avoid differential operations. This can be obtained by moving the term containing x_2 in Equation (19) to the left side of the equation:

$$\begin{cases} \dot{z}_2 - l_2 \dot{x}_1 = z_3 + b_{p0} u - l_2 z_2 \\ \dot{z}_3 - l_3 \dot{x}_1 = -l_3 z_2 \end{cases} \quad (21)$$

The new state variable is introduced such that:

$$\begin{cases} \bar{z}_2 = z_2 - l_2 x_1 \\ \bar{z}_3 = z_3 - l_3 x_1 \end{cases} \quad (22)$$

According to Equation (21) and Equation (22), the state equation can be obtained as:

$$\begin{cases} \dot{\bar{z}}_2 = \bar{z}_3 + l_3 x_1 + b_{p0} u - l_2 (\bar{z}_2 + l_2 x_1) \\ \dot{\bar{z}}_3 = -l_3 (\bar{z}_2 + l_2 x_1) \end{cases} \quad (23)$$

According to the pole configuration method, the poles of the observer are configured to $-\omega_o$, which gives an observer gain of:

$$l_2 = 2\omega_o, l_3 = \omega_o^2 \quad (24)$$

If the reconfigured RESO can observe \bar{z}_2, \bar{z}_3 correctly, then z_1 and z_2 can be inversely found according to Equation (22), and f_p can be found according to Equation (16). The simplified control block diagram of GFM power decoupling based on RESO is shown in Figure 4. The compensation amount of decoupling is designed as follows:

$$\begin{cases} \Delta\delta_c = f_p / b_{p0} \\ \Delta E_c = f_q / b_{q0} \end{cases} \quad (25)$$

As an example, the active power ring control loop is obtained by bringing Equation (25) into Equation (13) in conjunction with Figure 4:

$$\begin{aligned} \Delta\ddot{P} + a_2\Delta\dot{P} + a_1\Delta P &= b_{p0}\Delta\delta + f_p \\ &= b_{p0}(\Delta\delta_o - \Delta\delta_c) + f_p \\ &= b_{p0}(\Delta\delta_o - f_p/b_{p0}) + f_p \\ &= b_{p0}\Delta\delta_o \end{aligned} \quad (26)$$

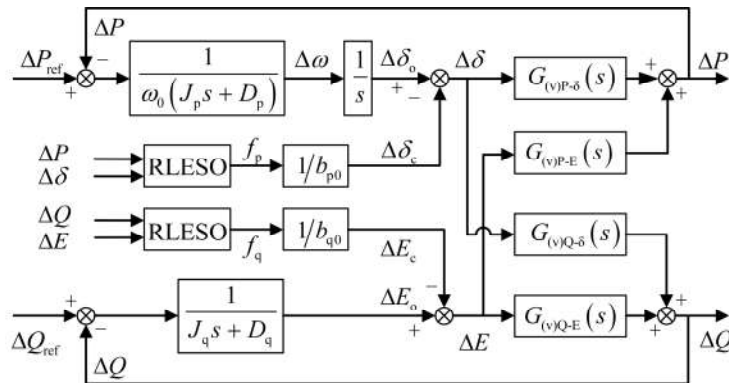


Figure 4. Simplified control block diagram of GFM power decoupling based on RESO.

The model deviation due to line impedance parameter perturbation and the disturbance f_p of power coupling are accurately estimated by RESO, and the disturbance compensation strategy is implemented based on typical power control strategy and virtual impedance decoupling. When the deviation of the actual line impedance parameters occurs, the power coupling can be suppressed, and the independent control of active and reactive power can be realized.

3.2. Frequency Domain Analysis of ESO Disturbance Estimation Performance

In order to analyze the performance of the ESO for disturbance estimation, two transfer functions from the actual total disturbance x_3 to the observed total disturbance z_3 of the ESO are established, as well as the transfer function from the actual total disturbance x_3 to the total disturbance estimation error $e_3 = z_3 - x_3$. Based on the derived transfer functions, the ESO can be analyzed from the frequency domain perspective.

(1) Transfer function of the total disturbance z_3 observed by ESO to the actual total disturbance x_3

By associating (17) with Equation (18), it can be obtained:

$$\begin{cases} \dot{x}_1 = x_2 \\ \dot{x}_2 = x_3 + b_{p0}u \\ \dot{z}_1 = z_2 + \beta_1(x_1 - z_1) \\ \dot{z}_2 = z_3 + b_{p0}u + \beta_2(x_1 - z_1) \\ \dot{z}_3 = \beta_3(x_1 - z_1) \end{cases} \quad (27)$$

The Laplace transform of Equation (27) yields a transfer function from the actual total disturbance x_3 to the observed total disturbance z_3 as:

$$H_1(s) = \frac{z_3(s)}{x_3(s)} = \frac{\beta_3}{s^3 + \beta_1 s^2 + \beta_2 s + \beta_3} \quad (28)$$

Let $V_1(s) = H_1(s) - 1$ be the transfer function from the actual total disturbance x_3 to the total disturbance estimation error e_3 .

(2) The transfer function of the total disturbance z_3 observed by the reduced-order ESO to the actual total disturbance x_3

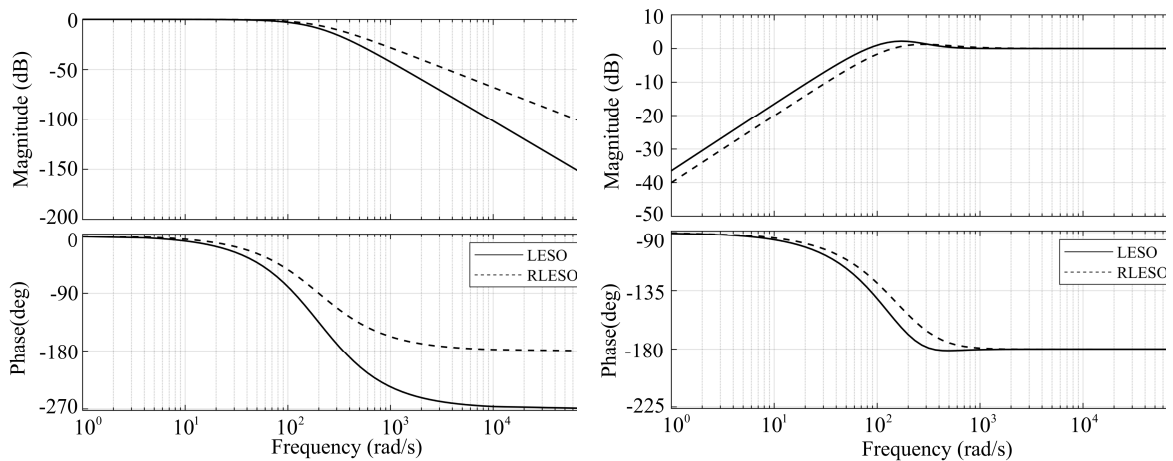
by associating (17) with Equation (20), can be obtained:

$$\begin{cases} \dot{x}_2 = x_3 + b_0 u \\ \dot{z}_2 = z_3 + b_0 u + l_2(x_2 - z_2) \\ \dot{z}_3 = l_3(x_2 - z_2) \end{cases} \quad (29)$$

The Laplace transform of Equation (29) yields a transfer function from the actual total disturbance x_3 to the observed total disturbance z_3 as:

Let $V_2(s) = H_2(s) - 1$ be the transfer function from the actual total disturbance x_3 to the total disturbance estimation error e_3 .

According to the pole configuration method, the poles of the two ESOs are configured at the same position, and taking $\omega_o = 200$ rad/s, the Bird's plots of $V(s)$ and $H(s)$ of the two ESOs can be obtained, as shown in Figure 5. According to Figure 5(a), from the amplitude-frequency curve, the third-order ESO has a stronger suppression ability for high-frequency disturbances; however, from the phase-frequency curve, the third-order ESO has an obvious phase lag, which will lead to a delay in its response to the disturbances of the observed system, and consequently weakening the compensation effect of the disturbances, and the phase lag of the reduced-order ESO is obviously reduced. From Figure 5(b), it can be seen that the estimation error of the reduced-order ESO is more minor in the low-frequency band.



(a) Frequency domain curve from x_3 to z_3

(b) Frequency domain curve from x_3 to e_3

Figure 5. Frequency domain analysis of observation capabilities of different ESOs.

Taking $\omega_0=200,400,800$ rad/s, respectively, the Bird's plots of $V_2(s)$ and $H_2(s)$ of the RESO with different bandwidths can be obtained, as shown in Figure 6. From Figure 6(a), it can be seen that the RESO has the ability to suppress high-frequency disturbances, but with the increase of the bandwidth, it has the ability to suppress high-frequency disturbances gradually deteriorates; from the phase-frequency curves, with the increase of the bandwidth, the phase lag of the RESO will gradually decrease. From Figure 6(b), it can be seen that the estimation error of RESO is very small for the disturbance in the low frequency band, and as the bandwidth increases, the estimation error of RESO for the disturbance in the low-frequency band gets smaller and smaller; however, as the frequency of the disturbed signal increases, the estimation ability of RESO gets worse and worse, and when the frequency of the disturbed signal reaches a certain degree, RESO will not be able to estimate it at all.

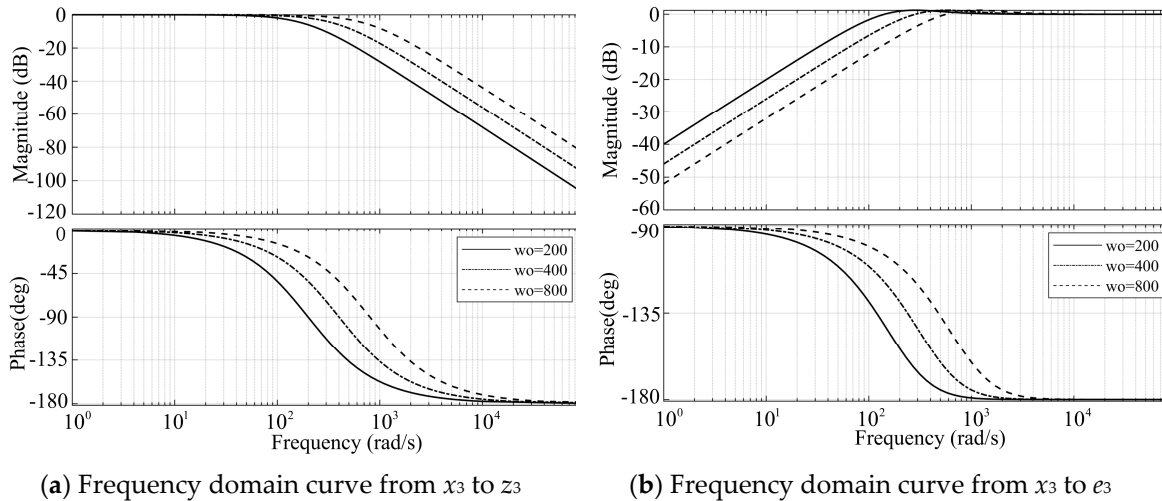


Figure 6. Frequency domain analysis of RESO observation capability for different bandwidths.

4. Hardware-in-the-Loop Experimental Verification

In order to further verify the effectiveness of the proposed control strategy, a hardware-in-the-loop experimental model of the grid-forming inverter with a structure corresponding to Figure 1 is constructed. As shown in Figure 7, the hardware-in-the-loop system consists of two parts: the controller and the RT Box. The controller adopts the chip TMS320F28379D control board, which is connected to the RT Box through the interface board, and the sampling data are also sent to the oscilloscope through the ports on the interface board to display the waveforms. The RT Box is able to perform real-time simulation of the hardware physical circuits, and is connected to the host computer through Gigabit Ethernet to realize data interaction. The size of the line impedance in the low-voltage micro-network is $R_g=0.642\Omega/\text{km}$, $X_g=0.083\Omega/\text{km}$, and the impedance ratio is $R/X=7.7$ [37]. The nominal line impedance is selected as the length of the line is 5km, and the actual line impedance cases are designed as follows: (1) +10% perturbation of the resistance parameter, +10% perturbation of the inductance parameter; (2) +20% perturbation of resistance parameter, +20% perturbation of inductance parameter; (3) +10% perturbation of the resistance parameter, -10% perturbation of the inductance parameter; (4) +20% perturbation of resistance parameter, -20% perturbation of inductance parameter. The main parameters of hardware-in-the-loop are shown in Table 1. The main parameters of the controller are shown in Table 2.

Table 1. Hardware-in-the-loop main parameter.

Parameters	Value /unit
Grid phase voltage (RMS)	220 V
DC bus voltage	750 V
grid frequency	50 Hz
Inverter side Inductance	2 mH

Network side Inductance	0.4 mH
filter capacitor	2.2 uF
Nominal line Inductance	1.32 mH
Nominal line resistance	3.21 Ω
Virtual Inductors	5 mH
Virtual Resistors	-3 Ω
switching frequency	100 kHz
Plant discretization time-step	500 ns

Table 2. Controller parameter.

Parameters	Value
Current inner loop proportional gain	5
Voltage outer loop proportional gain	0.01
Voltage outer loop integration gain	300
Active power observer bandwidth	700 rad/s
Reactive power observer bandwidth	500 rad/s
Virtual Inductors	5 mH
Virtual Resistors	-3 Ω
Virtual inertia factor for active power	0.04
Active droop factor	10.07
Virtual inertia factor for reactive power	5
Reactive droop factor	321.5

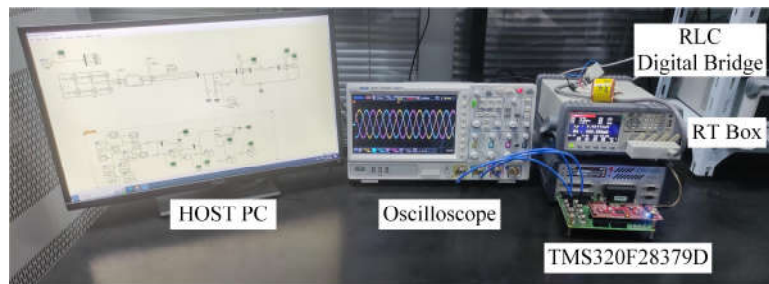


Figure 7. Hardware-in-the-loop experimental platform.

4.1. Verification of the Effect of Line Impedance Parameter Perturbation on Decoupling Ability

Under the initial state, the active power is 5 kW and the reactive power is 0 Var. Figure 8 shows that when the active power setting is increased from 5kW to 6kW, the reactive power changes by 1.7kVar. Since the nominal line impedance is mainly resistive, the power coupling phenomenon is more serious. Figure 9 shows that when using virtual impedance for decoupling, the set value of active power is also increased by 1kW, and the reactive power only changes by 230Var, which obviously reduces the coupling between active and reactive power. However, Figure 10 and 11 show that when the grid-forming inverter is operated at the actual line impedance, the active power set value is increased by the same 1kW, the reactive power changes 430Var in Case 1, and the reactive power changes 680Var in Case 2. It can be seen that the decoupling ability of the virtual impedance method is affected by the line impedance parameter perturbation, which results in the decoupling ability becoming worse. The greater the range of deviation of the impedance parameter, the less effective the decoupling is.

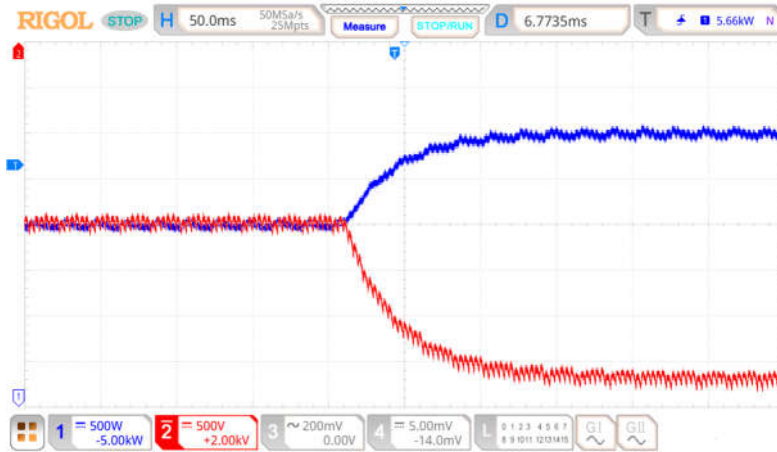


Figure 8. Without power decoupling (running at nominal line impedance).

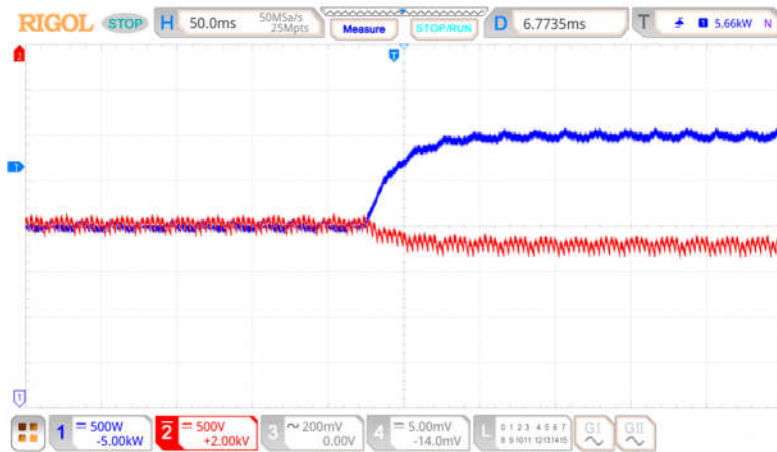


Figure 9. Power decoupling with virtual impedance method (running at nominal line impedance).

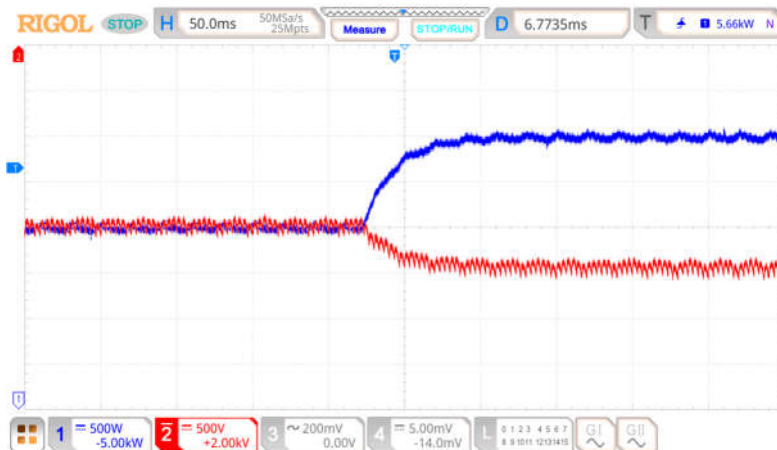


Figure 10. Power decoupling with virtual impedance method (running at actual line impedance Case 1).

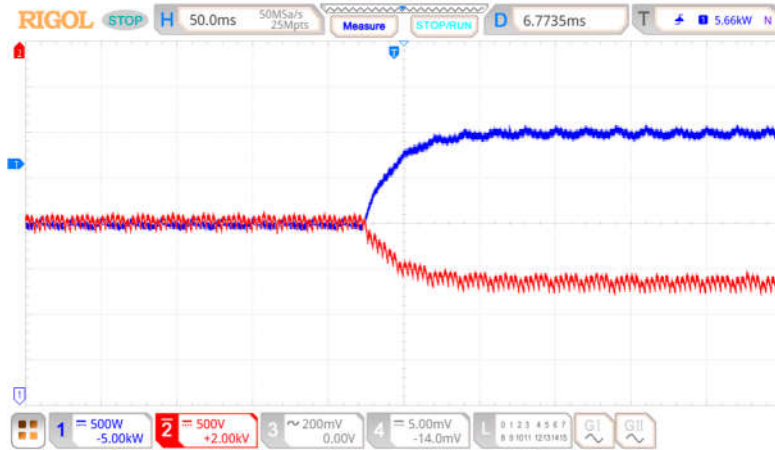


Figure 11. Power decoupling with virtual impedance method (running at actual line impedance Case 2).

4.2. Verification of ESO-Based Power Decoupling Control Strategy

Under the initial state, the active power is 5 kW, and the reactive power is 0 Var. The parameters of the power decoupling strategy based on RESO are designed at nominal line impedance. Figures 12–15 show that the reactive power changes by 100 Var for all four kinds of line impedance parameter perturbation conditions when the active power setpoint is increased from 5kW to 6kW. The RESO-based power decoupling strategy has better decoupling capability and more robust decoupling when the line impedance has different sizes of parameter perturbation.

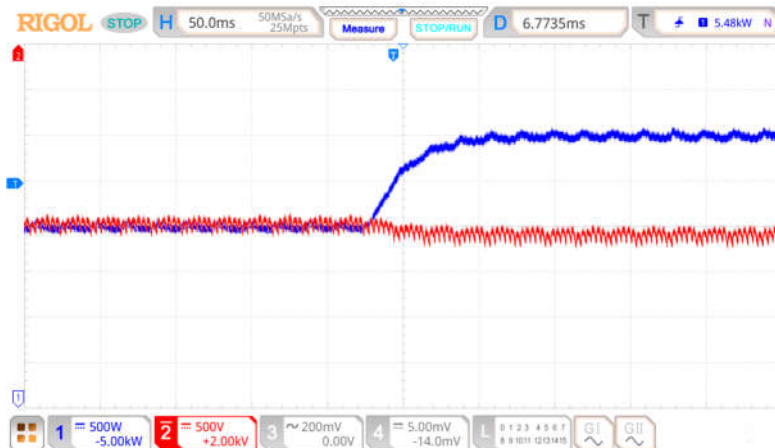


Figure 12. Power decoupling strategy based on RESO (running at actual line impedance Case 1, P change of 1kW).

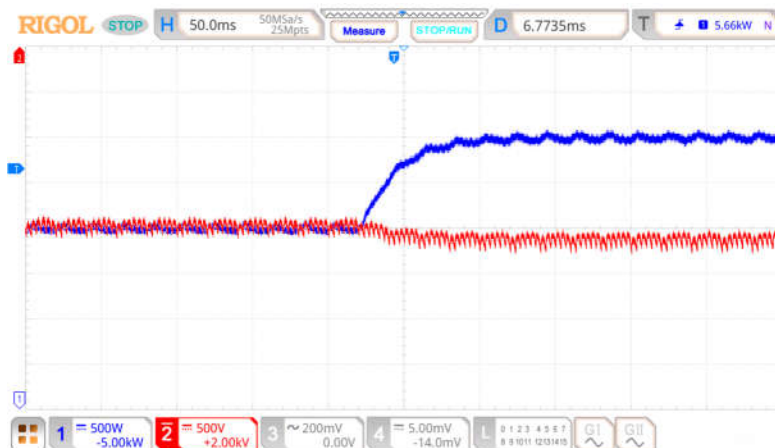


Figure 13. Power decoupling strategy based on RESO (running at actual line impedance Case 2, P change of 1kW).

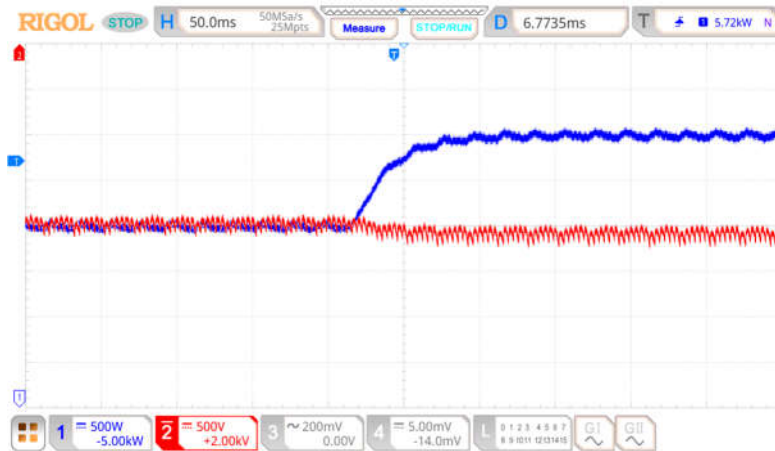


Figure 14. Power decoupling strategy based on RESO (running at actual line impedance Case 3, P change of 1kW).

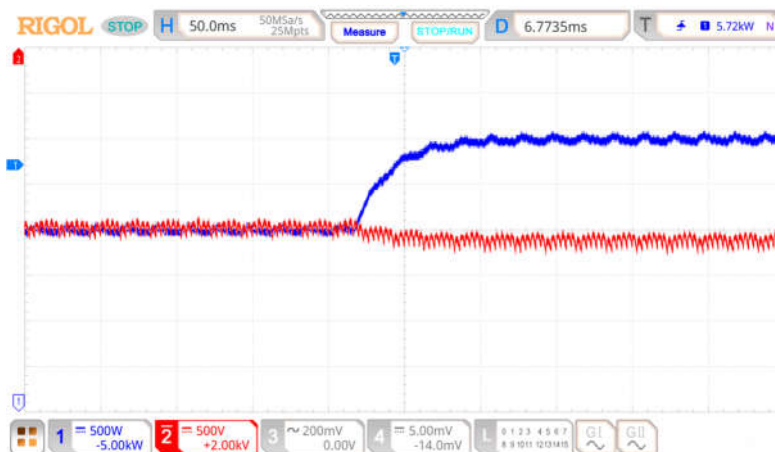


Figure 15. Power decoupling strategy based on RESO (running at actual line impedance Case 4, P change of 1kW).

5. Conclusions

In this paper, a power decoupling control strategy based on reduced-order ESO is proposed in order to improve the robustness of the GFM power decoupling control strategy when line impedance parameter perturbation occurs. The strategy considers the factors affecting the power control performance, such as model deviation and power coupling caused by line impedance parameter perturbation, as internal disturbances. Based on the typical power control strategy and virtual impedance method, these disturbances are observed and compensated in real-time by the reduced-order ESO. The reduced-order ESO reduces the computing power of the control system and decreases the phase delay of the system. Finally, through RT Box hardware-in-the-loop experimental verification, it is demonstrated that the power decoupling control strategy based on the reduced-order ESO has better decoupling ability and improves the robustness of the power decoupling control when the line impedance parameter perturbation.

Author Contributions: Conceptualization, M.H.; methodology, M.H. and H.L.; software, M.H.; validation, M.H.; formal analysis, M.H. and H.L.; writing—original draft preparation, M.H.; writing—review and editing, M.H. and H.L.; visualization, M.H.; supervision, M.H. and H.L. All authors have read and agreed to the published version of the manuscript.

Funding: This research was supported by Shanghai Science and Technology Commission Key Program (grant no. 20dz1206100).

Data Availability Statement: Data is unavailable due to privacy.

Conflicts of Interest: All authors claim that this study was conducted without any commercial or financial activities relationships that may be interpreted as potential conflicts of interest.

References

1. Zhao, G.; Yang, H. Parallel Control of Converters with Energy Storage Equipment in a Microgrid. *Electronics* 2019, 8, 1110, doi:10.3390/electronics8101110.
2. Matevosyan, J.; Badrzadeh, B.; Prevost, T.; Quitmann, E.; Ramasubramanian, D.; Urdal, H.; Achilles, S.; MacDowell, J.; Hsien Huang, S.; Vital, V.; et al. Grid-Forming Inverters: Are They the Key for High Renewable Penetration? *IEEE Power and Energy Magazine* 2023, 21, 77–86, doi:10.1109/MPAE.2023.10083082.
3. Chen, Y.; Luo, J.; Zhang, X.; Li, X.; Wang, W.; Ding, S. A Virtual Synchronous Generator Secondary Frequency Modulation Control Method Based on Active Disturbance Rejection Controller. *Electronics* 2023, 12, 4587, doi:10.3390/electronics12224587.
4. Wang, L.; Zhou, H.; Hu, X.; Hou, X.; Su, C.; Sun, K. Adaptive Inertia and Damping Coordination (AIDC) Control for Grid-Forming VSG to Improve Transient Stability. *Electronics* 2023, 12, 2060, doi:10.3390/electronics12092060.
5. Rosso, R.; Wang, X.; Liserre, M.; Lu, X.; Engelken, S. Grid-Forming Converters: Control Approaches, Grid-Synchronization, and Future Trends—A Review. *IEEE Open Journal of Industry Applications* 2021, 2, 93–109, doi:10.1109/OJIA.2021.3074028.
6. Arghir, C.; Jouini, T.; Dörfler, F. Grid-Forming Control for Power Converters Based on Matching of Synchronous Machines. *Automatica* 2018, 95, 273–282, doi:10.1016/j.automatica.2018.05.037.
7. Garzon, O.D.; Nassif, A.B.; Rahmatian, M. Grid Forming Technologies to Improve Rate of Change in Frequency and Frequency Nadir: Analysis-Based Replicated Load Shedding Events. *Electronics* 2024, 13, 1120, doi:10.3390/electronics13061120.
8. Johnson, B.B.; Sinha, M.; Ainsworth, N.G.; Dörfler, F.; Dhople, S.V. Synthesizing Virtual Oscillators to Control Islanded Inverters. *IEEE Transactions on Power Electronics* 2016, 31, 6002–6015, doi:10.1109/TPEL.2015.2497217.
9. Unruh, P.; Nuschke, M.; Strauß, P.; Welck, F. Overview on Grid-Forming Inverter Control Methods. *Energies* 2020, 13, 2589, doi:10.3390/en13102589.
10. Hu, P.; Jiang, K.; Ji, X.; Cai, Y.; Wang, B.; Liu, D.; Cao, K.; Wang, W. A Novel Grid-Forming Strategy for Self-Synchronous PMSG under Nearly 100% Renewable Electricity. *Energies* 2023, 16, 6648, doi:10.3390/en16186648.
11. Sun, Z.; Zhu, F.; Cao, X. Study on a Frequency Fluctuation Attenuation Method for the Parallel Multi-VSG System. *Front. Energy Res.* 2021, 9, doi:10.3389/fenrg.2021.693878.
12. Shang, L.; Hu, J.; Yuan, X.; Chi, Y.; Tang, H. Modeling and Improved Control of Virtual Synchronous Generators Under Symmetrical Faults of Grid. *Zhongguo Dianji Gongcheng Xuebao/Proceedings of the Chinese Society of Electrical Engineering* 2017, 37, 403–411, doi:10.13334/j.0258-8013.pcsee.162201.
13. Jiang, K.; Liu, D.; Cao, K.; Xiong, P.; Ji, X. Small-Signal Modeling and Configuration Analysis of Grid-Forming Converter under 100% Renewable Electricity Systems. *Electronics* 2023, 12, 4078, doi:10.3390/electronics12194078.
14. Song, Z.; Zhang, J.; Tang, F.; Wu, M.; Lv, Z.; Sun, L.; Zhao, T. Small Signal Modeling and Parameter Design of Virtual Synchronous Generator to Weak Grid. In *Proceedings of the 2018 13th IEEE Conference on Industrial Electronics and Applications (ICIEA)*; May 2018; pp. 2618–2624.
15. Wu, H.; Ruan, X.; Yang, D.; Chen, X.; Zhao, W.; Lv, Z.; Zhong, Q.-C. Small-Signal Modeling and Parameters Design for Virtual Synchronous Generators. *IEEE Transactions on Industrial Electronics* 2016, 63, 4292–4303, doi:10.1109/TIE.2016.2543181.
16. Sarojini, R.K.; Palanisamy, K. Small Signal Modelling and Determination of Critical Value of Inertia for Virtual Synchronous Generator. In *Proceedings of the 2019 Innovations in Power and Advanced Computing Technologies (i-PACT)*; March 2019; Vol. 1, pp. 1–6.

17. Yu, J.; Qi, Y.; Deng, H.; Liu, X.; Tang, Y. Evaluating Small-Signal Synchronization Stability of Grid-Forming Converter: A Geometrical Approach. *IEEE Transactions on Industrial Electronics* 2022, 69, 9087–9098, doi:10.1109/TIE.2021.3113000.
18. Zhang, L.; Harnefors, L.; Nee, H.-P. Power-Synchronization Control of Grid-Connected Voltage-Source Converters. *IEEE Transactions on Power Systems* 2010, 25, 809–820, doi:10.1109/TPWRS.2009.2032231.
19. D'Arco, S.; Suul, J.A.; Fosso, O.B. Small-Signal Modelling and Parametric Sensitivity of a Virtual Synchronous Machine. In *Proceedings of the 2014 Power Systems Computation Conference*; August 2014; pp. 1–9.
20. Stankovic, A.M.; Sanders, S.R.; Aydin, T. Dynamic Phasors in Modeling and Analysis of Unbalanced Polyphase AC Machines. *IEEE Transactions on Energy Conversion* 2002, 17, 107–113, doi:10.1109/60.986446.
21. Wu, T.; Liu, Z.; Liu, J.; Wang, S.; You, Z. A Unified Virtual Power Decoupling Method for Droop-Controlled Parallel Inverters in Microgrids. *IEEE Transactions on Power Electronics* 2016, 31, 5587–5603, doi:10.1109/TPEL.2015.2497972.
22. De Brabandere, K.; Bolsens, B.; Van den Keybus, J.; Woyte, A.; Driesen, J.; Belmans, R. A Voltage and Frequency Droop Control Method for Parallel Inverters. *IEEE Transactions on Power Electronics* 2007, 22, 1107–1115, doi:10.1109/TPEL.2007.900456.
23. Li, Y.; Li, Y.W. Power Management of Inverter Interfaced Autonomous Microgrid Based on Virtual Frequency-Voltage Frame. *IEEE Transactions on Smart Grid* 2011, 2, 30–40, doi:10.1109/TSG.2010.2095046.
24. Peng, Z.; Wang, J.; Bi, D.; Wen, Y.; Dai, Y.; Yin, X.; Shen, Z.J. Droop Control Strategy Incorporating Coupling Compensation and Virtual Impedance for Microgrid Application. *IEEE Transactions on Energy Conversion* 2019, 34, 277–291, doi:10.1109/TEC.2019.2892621.
25. Peng, Z.; Wang, J.; Wen, Y.; Bi, D.; Dai, Y.; Ning, Y. Virtual Synchronous Generator Control Strategy Incorporating Improved Governor Control and Coupling Compensation for AC Microgrid. *IET Power Electronics* 2019, 12, doi:10.1049/iet-pel.2018.6167.
26. Li, C.; Yang, Y.; Mijatovic, N.; Dragicevic, T. Frequency Stability Assessment of Grid-Forming VSG in Framework of MPME With Feedforward Decoupling Control Strategy. *IEEE Transactions on Industrial Electronics* 2022, 69, 6903–6913, doi:10.1109/TIE.2021.3099236.
27. Rathnayake, D.B.; Bahrani, B. Multivariable Control Design for Grid-Forming Inverters With Decoupled Active and Reactive Power Loops. *IEEE Transactions on Power Electronics* 2023, 38, 1635–1649, doi:10.1109/TPEL.2022.3213692.
28. Guerrero, J.M.; Vicuna, L.G. de; Matas, J.; Castilla, M.; Miret, J. Output Impedance Design of Parallel-Connected UPS Inverters with Wireless Load-Sharing Control. *IEEE Transactions on Industrial Electronics* 2005, 52, 1126–1135, doi:10.1109/TIE.2005.851634.
29. Rodríguez-Cabero, A.; Roldán-Pérez, J.; Prodanovic, M. Virtual Impedance Design Considerations for Virtual Synchronous Machines in Weak Grids. *IEEE Journal of Emerging and Selected Topics in Power Electronics* 2020, 8, 1477–1489, doi:10.1109/JESTPE.2019.2912071.
30. Wen, T.; Zhu, D.; Zou, X.; Jiang, B.; Peng, L.; Kang, Y. Power Coupling Mechanism Analysis and Improved Decoupling Control for Virtual Synchronous Generator. *IEEE Transactions on Power Electronics* 2021, 36, 3028–3041, doi:10.1109/TPEL.2020.3017254.
31. He, J.; Li, Y.W. Analysis, Design, and Implementation of Virtual Impedance for Power Electronics Interfaced Distributed Generation. *IEEE Transactions on Industry Applications* 2011, 47, 2525–2538, doi:10.1109/TIA.2011.2168592.
32. Wang, Y.; Wai, R.-J. Newly-Designed Power Decoupling Strategy for Virtual Synchronous Generator in Micro-Grid. In *Proceedings of the 2021 IEEE International Future Energy Electronics Conference (IFEEEC)*; November 2021; pp. 1–6.
33. Wang, Y.; Wai, R.-J. Adaptive Fuzzy-Neural-Network Power Decoupling Strategy for Virtual Synchronous Generator in Micro-Grid. *IEEE Transactions on Power Electronics* 2022, 37, 3878–3891, doi:10.1109/TPEL.2021.3120519.
34. Dong, N.; Li, M.; Chang, X.; Zhang, W.; Yang, H.; Zhao, R. Robust Power Decoupling Based on Feedforward Decoupling and Extended State Observers for Virtual Synchronous Generator in Weak Grid. *IEEE Journal of Emerging and Selected Topics in Power Electronics* 2023, 11, 576–587, doi:10.1109/JESTPE.2022.3207973.

35. Han, J. From PID to Active Disturbance Rejection Control. IEEE Transactions on Industrial Electronics 2009, 56, 900–906, doi:10.1109/TIE.2008.2011621.
36. Fu, C.; Tan, W. Parameters Tuning of Reduced-Order Active Disturbance Rejection Control. IEEE Access 2020, 8, 72528–72536, doi:10.1109/ACCESS.2020.2987398.
37. Engler, A.; Soultanis, N. Droop Control in LV-Grids. In Proceedings of the 2005 International Conference on Future Power Systems; November 2005; p. 6 pp. – 6.

Disclaimer/Publisher's Note: The statements, opinions and data contained in all publications are solely those of the individual author(s) and contributor(s) and not of MDPI and/or the editor(s). MDPI and/or the editor(s) disclaim responsibility for any injury to people or property resulting from any ideas, methods, instructions or products referred to in the content.